Applied Surface Science 565 (2021) 150152

Contents lists available at ScienceDirect

Applied Surface Science

journal homepage: www.elsevier.com/locate/apsusc

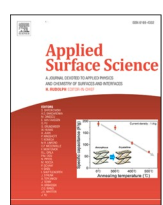

Full Length Article

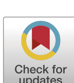

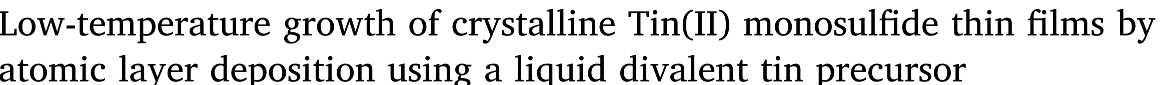

Low-temperature growth of crystalline Tin(II) monosulfide thin films by atomic layer deposition using a liquid divalent tin precursor

Mohd Zahid Ansari [a], Petr Janicek [b,c], Dip K. Nandi [a], Stanislav Slang [c], Marek Bouska [c,d], Hongjun Oh [e], Bonggeun Shong [e], Soo-Hyun Kim [a,f,*]

[a] School of Materials Science and Engineering, Yeungnam University, 280 Daehak-Ro, Gyeongsan, Gyeongbuk 38541, Republic of Korea
[b] Institute of Applied Physics and Mathematics, Faculty of Chemical Technology, University of Pardubice, Studentska 95, Pardubice 532 10 Czech Republic
[c] Center of Materials and Nanotechnologies, Faculty of Chemical Technology, University of Pardubice, Studentska 95, Pardubice 532 10, Czech Republic
[d] Department of Graphic Arts and Photophysics, Faculty of Chemical Technology, University of Pardubice, Studentska 95, Pardubice 532 10, Czech Republic
[e] Department of Chemical Engineering, Hongik University, 94 Wausan-ro, Mapo-gu, Seoul 04066, Republic of Korea
[f] Institute of Materials Technology, Yeungnam University, Yeungnam University, 280 Daehak-Ro, Gyeongsan, Gyeongbuk 38541, Republic of Korea

ARTICLE INFO

Keywords:
Atomic layer deposition
Tin monosulfide
Sn (II) precursor
Density functional theory
Spectroscopic ellipsometry

ABSTRACT

In this study, better-quality stoichiometric SnS thin films were prepared by atomic layer deposition (ALD) using a liquid divalent Sn precursor, N, N′-di-*t*-butyl-2-methylpropane-1,2-diamido tin(II) [Sn(dmpa)], and H_2S. A relatively high growth per ALD cycle (GPC) value of approximately 0.13 nm/cycle was achieved at 125 °C. Furthermore, crystalline SnS films could be grown from room temperature (25 °C) to a high temperature of 250 °C. Density functional theory (DFT) calculations were used to examine the surface reactions and self-limiting nature of the Sn precursor. Mixed phases of cubic (π) and orthorhombic (o) SnS films were deposited at low temperatures (25–100 °C), whereas only the orthorhombic phase prevailed at high growth temperatures (>125 °C) based on the complementary results of X-ray diffractometry (XRD), Raman spectroscopy, and X-ray photoelectron spectroscopy (XPS) analyses. The optoelectronic properties of the SnS films were further evaluated by spectroscopic ellipsometry (SE) analysis. The results from the SE analysis supported the observed change from mixed π-SnS and o-SnS to o-SnS with increasing deposition temperature and allowed the determination of the energy bandgap (~1.1 eV) and a relatively broad semi-transparent window (up to 3000 nm). Overall, this new ALD process for obtaining a good quality SnS is applicable even at room temperature (25 °C), and we foresee that this process could be of considerable interest for emerging applications.

1. Introduction

Metal chalcogenides have recently emerged as materials of great interest for a wide range of applications, owing to their admirable physicochemical properties [1,2]. Of particular note, SnS is considered one of the most researched metal chalcogenide compounds in the form of both powder and thin films owing to its abundance, nontoxic nature, and attractive opto-electrical properties [3–15]. SnS crystallizes with an orthorhombic crystal geometry (*Pnma* space group), where each Sn(II) atom is linked to six S chalcogen atoms, forming a highly distorted octahedral structure to form a two-layered structure [3,16–21,23–27]. These adjacent S layers with a larger interlayer spacing (0.43 nm) are associated by weak van der Waals forces, which are of particular interest for the intercalation of Na + and Li + while alleviating the effect of structural deformation [1–3]. SnS is a p-type semiconductor with good hole mobility (90–500 cm^2/V), high free carrier concentration (10^{17}–10^{18} cm^{-3}), and a high absorption coefficient (>10^4 cm^{-1}) with a band gap of 1.1–1.8 eV [2,3,5]. SnS could also form a cubic crystalline structure with a larger lattice constant ($a = 11.6$ Å), which was initially known as a zinc blende structure, with a band gap of 1.7 eV [11–21].

Despite the excellent properties SnS has, it is difficult to achieve because of the formation of tin sulfides with different stoichiometries (like SnS_2, Sn_2S_3), resulting in the failure to obtain phase-pure Sn(II) sulfide [19,42]. For example, existing SnS-based solar cells have achieved efficiencies of only approximately 5%, whereas theoretical studies suggest an achievable efficiency of approximately 24% [19]. One of the major concern in this regard is to achieve impurity (like oxide) and secondary phase-free SnS [2–4,19,23–31]. As can be seen in the Table S1

* Corresponding author at: School of Materials Science and Engineering, Yeungnam University, 280 Daehak-Ro, Gyeongsan, Gyeongbuk 38541, Republic of Korea.
E-mail address: soohyun@ynu.ac.kr (S.-H. Kim).

https://doi.org/10.1016/j.apsusc.2021.150152
Received 16 March 2021; Received in revised form 27 April 2021; Accepted 15 May 2021
Available online 9 July 2021
0169-4332/© 2021 Elsevier B.V. All rights reserved.

[22], secondary phases (Sn_2S_3 and SnS_2) are often deposited owing to the higher stability of Sn + 4 than the + 2 oxidation state. The uniformity of single-phase SnS films is also compromised at higher temperatures. In addition, high surface roughness is observed in SnS films prepared at such high temperatures [19]. Moreover, the frequently used methods like physical and chemical vapor deposition (PVD and CVD) to deposit SnS thin films often suffer from essential limitations such as poor uniformity of film thickness, phase purity, reproducibility of the films, and step coverage (Table S1) [22]. In this context, atomic layer deposition (ALD), a modified version of CVD, is of particular interest for preparing uniform and conformal thin films owing to its self-limiting surface reaction during alternating exposure of precursors [32,33]. ALD also enables precise control of the film thickness, even up to a few nm, and the properties of ALD films, including composition, and phase, can easily be altered through the use of various ALD precursors and different process parameters.

In this regard, ALD tin sulfide is being studied more closely [33–45]. In addition to their promise for solar cell applications, ALD-SnS films have also been successfully utilized in various other applications [33,40,42,44]. To the best of our knowledge, five varieties of Sn (II) precursors have been reported so far as shown in the Table S2 [22]. Sn (II) compounds make it easy to produce Sn(II) sulfide by avoiding the formation of Sn(IV) sulfide. Additionally, the use of a divalent Sn precursor widens the deposition temperature range for growing pure SnS as compared to the tetravalent Sn precursor [37]. Tin(II) 2,4-pentanedionate [$Sn(acac)_2$] [34], bis(N,N′-diisopropylacetamidinato) tin(II) [$Sn(amd)_2$] [36], N,N′-di-*tert*-butyl-2,3-diamidobutanetin (II) [Sn(dbdib)] [41], bis(1-dimethylamino-2-methyl-2-propoxy)tin(II) [Sn(dmamp)] [42], and bis(N,N′ diisopropylformamidinato) tin(II) [Sn(dipfamd)] [44] are the studied tin precursors. Their molecular structures are shown in Table 1 [44]. ALD of SnS was first reported by Kim et al. using $Sn(acac)_2$ and H_2S at temperatures ranging from 125 to 225 °C with a low growth per cycle (GPC) of 0.24 Å [34]. The films contained substantial oxygen residue of approximately 20% as the acac ligand had an oxygen molecule. In another study, the ALD-SnS process was established using Sn(II)(dmamp) precursor at temperatures of 90–240 °C with a low GPC of 0.36 Å [42]. A relatively higher GPC of 0.86 Å for ALD-SnS was reported with an amidinate-based solid precursor, $Sn(II)(dipamd)_2$, which yielded only the orthorhombic phase in the 100–200 °C range [36]. Recently, another ALD process using an amidinate-based Sn(II) precursor, Sn(II)(dipfamd), was reported for orthorhombic and cubic mixed phase SnS films deposited at temperatures from 65 to 180 °C; [44] the authors claimed that the diisopropylformamidinate ligand enhanced both volatility and reactivity of the precursor compared to diisopropylacetamidinate congeners. Kim et al. reported that cyclic amide-based precursors were more volatile than amidinate-based precursors and hence, might bring down the deposition even further.[41] The process involving cyclic amide based precursor, Sn(dbdib), demonstrated that SnS deposition is possible at a low temperature of 50 °C with a high GPC of 1.25 Å [41]. Thus far, this cyclic-based Sn(II) precursor, has better growth properties than other known Sn(II) precursors, which have complex symmetrical or planar structures and are in a solid state with low processability (low GPC and poor repeatability). Therefore, the precursor selection plays a significant role in establishing the growth temperature, the ALD process performance as represented by GPC, and even the material properties of the deposited films. Hence, it is worthwhile to continue the development of new precursors to discover the properties of low-temperature SnS films by optimizing the growth parameters for a particular application.

Herein, we present a thermal ALD of SnS using a newly synthesized cyclic amide based liquid tin(II) precursor, [N, N′-di-*t*-butyl-2-methylpropane-1,2-diamido tin(II), Sn(dmpa)], and H_2S. Cyclic amide compounds were introduced by adding an asymmetric ligand to induce a nonplanar or asymmetric structure. This made it possible to prepare a liquid precursor, which can improve the volatility significantly because the intermolecular force is weak compared to that of a solid material at room temperature. Tuning intermolecular force was performed by changing the carbon position of the existing compound without changing the molecular weight [43]. Typical ALD related growth kinetics were explored and discussed. Density functional theory (DFT) calculations showed the feasible surface reaction mechanism of the precursor and H_2S, as well as possible self-limiting behavior. The as-grown SnS films were systematically analyzed in terms of their crystallographic nature, composition, microstructure, surface structure/morphology, and opto-electrical properties.

2. Materials and method

2.1. Materials preparations

SnS thin films were grown using [*N,N′*-di-*t*-butyl-2-methylpropane-1,2-diamido)tin(II), Sn(dmpa)] (Hansol Chemical, Republic of Korea) as the tin precursor (Table 1) and H_2S as the S source by ALD in a traveling wave-type thermal ALD reactor (Lucida-D100, NCD Technology) within a deposition temperature range of 25–250 °C. A stable pressure of 0.08 Torr was maintained in the ALD chamber. Sn(dmpa) is a liquid under ambient conditions; an appropriate vapor pressure was achieved by heating the precursor vessel to 40 °C. A liquid precursor has a certain advantage in terms of vapor pressure consistency, which is essential for reproducible ALD throughout the span of a precursor charge. This vapor pressure consistency is difficult to achieve for solid chemicals owing to their surface area variations. Silicon substrates covered by thermally deposited SiO_2 layer (~100 nm thickness) were utilized for the material characterization of the SnS thin films. A flow rate of 100 sccm was used to supply ultrahigh-purity Ar gas as the carrier to establish correct precursor delivery and to ensure a continuous 100 sccm flow for the purging gas between sequential exposures of Sn(dmpa) and H_2S. A constant 100 sccm flow of Ar was used for the pulsing H_2S gas as a reactant. Each ALD cycle consisted of the following sequential reaction schemes in the ALD-SnS process: Sn(dmpa) pulsing (2 s), purging (10 s), H_2S pulsing (2 s), and purging (10 s).

2.2. DFT calculations

DFT calculations were performed using periodic boundary conditions with the Vienna ab initio simulation package [46]. The PBE exchange–correlation functional was used with projector augmented-wave ultrasoft pseudopotentials and D3BJ dispersion correction. A plane-wave cutoff energy of 300 eV and a 3 × 3 × 1 Monkhorst–Pack k-point grid were used. Using this method, the unit cell parameters of

Table 1
The molecular structures of Sn(II) metalorganic precursors.

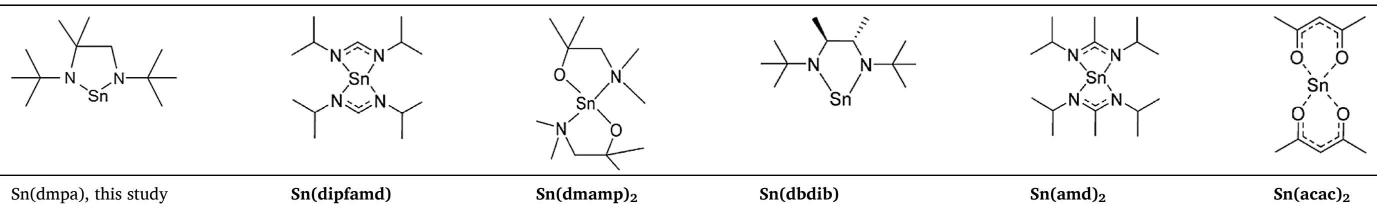

Sn(dmpa), this study	**Sn(dipfamd)**	**$Sn(dmamp)_2$**	**Sn(dbdib)**	**$Sn(amd)_2$**	**$Sn(acac)_2$**

monolayer orthorhombic SnS (Pnma) were optimized to $a = 3.98$ Å and $b = 4.40$ Å, which are close to the literature values of $a = 3.98$ Å and $b = 4.33$ Å (Crystallography Open Database ID: 1011253). A 3 × 3 supercell of monolayer SnS with an exposed surface orientation of (0 1 0) was constructed with a vacuum gap of 17 Å to avoid interactions between adjacent slabs. Two extreme coverages of thiol (–SH) groups were appended: one H adatom on one S atom of the supercell [θ(SH) = 1/9 monolayer: Figures S1(a, b), Supporting Information], and nine H_2S molecules dissociatively adsorbed on the supercell [(θ(SH) = 2 monolayers, Figure S1, Supporting Information). To obtain transition state structures, the climbing-image NEB (CI-NEB) method was used [47].

2.3. Materials characterizations

The ALD-SnS process was characterized by numerous methods to investigate the growth behavior and physical properties of the ALD-SnS film on the thermally grown SiO_2/Si substrate. The film thicknesses of the deposited SnS were calculated by cross-sectional-view scanning electron microscopy (SEM, HITACHI S-4800, and SEM, Tescan LYRA 3) and X-ray reflectance (XRR; PANalytical X′-pert PRO MRD with a Cu Kα source). Grazing-incidence angle X-ray diffraction (GIXRD, PANalytical X′-pert PRO MRD with an X-ray source of Cu Kα radiation) was done to explore the phase and crystalline properties of the SnS films. The surface morphology and root-mean-square roughness were identified using SEM and atomic force microscopy (AFM, DI Instruments NanoScope, Solver NEXT, NT-MDT) analysis. Further, stoichiometry and composition of Sn and S in the deposited films were identified using Rutherford backscattering spectrometry (incident energy of 2 MeV He^{2+} ions) via the RUMP simulation technique. X-ray photoelectron spectroscopy (XPS, Fisher Scientific Kα XPS spectrometer at the Korea Basic Science Institute at Busan, South Korea) was used to determine the chemical bonding states, oxidation conditions, elemental composition, and impurities contained in the SnS films. Top and cross-sectional view images were taken by transmission electron microscopy (TEM) and high-resolution TEM (Tecnai F20 armed with a 200 kV accelerating voltage)) to explore the crystalline nature and microstructure of the ALD-SnS film grown at 125 °C.

2.4. Ellipsometry analysis

The optoelectronic properties were characterized using two variable-angle spectroscopic ellipsometers (VASE and IR-VASE, J. A. Woollam). A rotating analyzer ellipsometer was operated in the spectral range of 190–1700 nm [ultraviolet–visible-near-infrared (UV–vis-NIR)]. Measurements with 25 analyzer revolutions with photon energy steps of 0.05 eV angles of incidence (AOI) of 50°, 55°, 60°, and 65° were performed for each sample. A rotating compensator ellipsometer covered the spectral range of 1.7–10 μm [NIR-MIR (mid-infrared)] and the same AOIs were recorded (25 scans, 15 spectra per revolution, with wavenumber steps of 8 cm^{-1}). The near-normal incidence optical reflectance was measured using the same instruments. WVASE32 software was performed to interpret the obtained data. A five-layer model of the sample structure consisting of Si, SiO_2, ALD-SnS layer, surface roughness, and air as ambient was used. The optical constants of Si and SiO_2 were used from the literature.[48] The Bruggeman effective medium approximation with 50% ALD-SnS and 50% air was applied to model surface roughness [49]. A homogenous layer was used to represent the ALD-SnS film as ALD is recognized to deposit high-quality uniform films.

3. Results and discussion

3.1. Growth kinetics and self-limiting growth of ALD-SnS process

First, we studied the film deposition at process temperatures varying from 25 to 250 °C while keeping the optimized pulse sequences unchanged. As displayed in Fig. 1(a), the growth rate was noticed to be 0.07 nm per cycle at 25 °C, and it increased slightly upon increasing the deposition temperature to 50 °C or higher. Interestingly, within a deposition temperature between 75 °C and 175 °C, the GPC exhibited negligible change (~0.12–0.13 nm per cycle), which clearly shows a considerable ALD temperature window for this process. However, beyond 175 °C, the GPC increased sharply, and at 250 °C, a very high

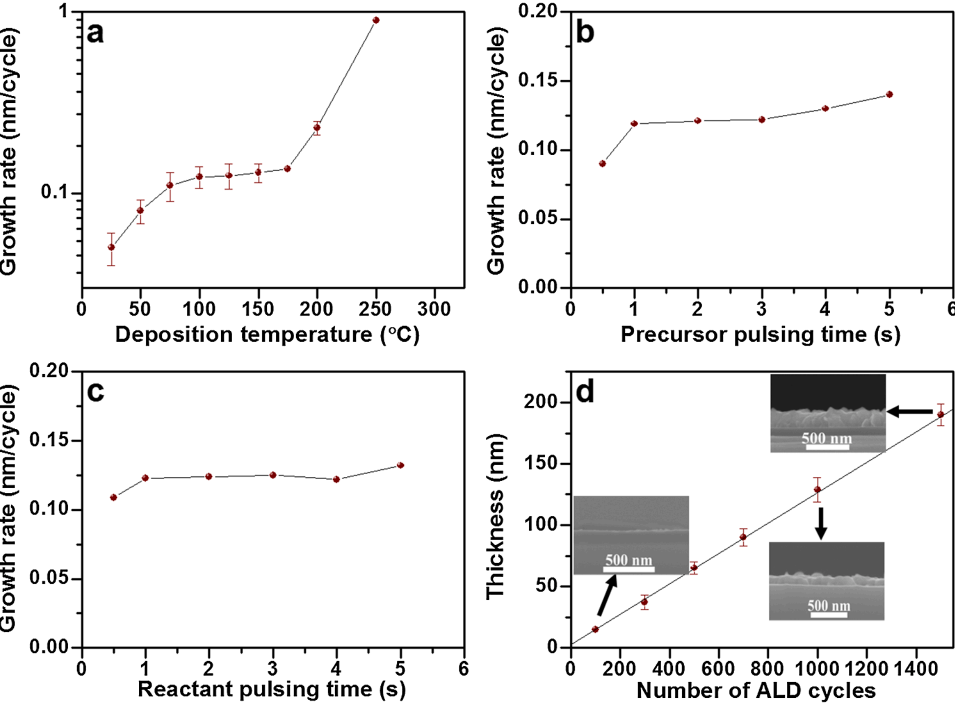

Fig. 1. Growth per cycle (GPC) of ALD-grown SnS films on thermally grown SiO_2/Si substrate (a) at various growth temperatures to define the ALD temperature window, (b) as a function of the precursor pulsing time, (c) reactant pulsing time, and (d) thicknesses of the films prepared with respect to the number of ALD cycles.

GPC value of 0.9 nm was detected. This temperature dependence of growth therefore indicates the onset of thermal decomposition above 175 °C, which becomes severe beyond 200 °C. It is worth noting that all reported precursors, excluding the less reactive one $[Sn(acac)]_2$, [29] show decreasing GPC values at increased temperatures. Once the temperature variation for ALD, as well as that for the CVD-type deposition behavior, was confirmed, we carried out film deposition within the ALD temperature frame for further study. To evaluate the growth mechanism of the present process, an ideal growth temperature of 125 °C was chosen by considering the ALD temperature window.

The self-limiting behavior of the film grown on the SiO_2/Si substrate was investigated with respect to the precursor and reactant exposure times, and the results are shown in Fig. 1(b) and (c), respectively. Upon varying the precursor exposure time, GPC initially increased from approximately 0.09 to 0.12 nm/cycle with increasing pulsing time from 0.5 to 1 s. However, the GPC became saturated at precursor dosing times above 1 s, whereas the pulsing time of H_2S was fixed at 2 s. Similarly, as shown in Fig. 1(c), by tuning the pulsing time of the H_2S reactant from 0.5 s to 5 s while keeping the pulsing time unchanged at 2 s, the GPC of the film initially increased with increasing reactant exposure and then reached saturation upon further H_2S exposure to 3 s. Therefore, this newly introduced metal–organic tin precursor displayed typical self-limiting behavior that was evident from the surface-saturated chemisorption of the precursors during ALD. A high GPC of approximately 0.13 nm/cycle was estimated for the current ALD-SnS process. Based on these outcomes, the basic pulsing conditions for both the precursor and reactant were set to 2 s, with a purging time of 10 s between the precursor–reactant pulse, ensuring self-limiting film growth. Furthermore, the linearity of the film's growth with increasing ALD cycles with almost no incubation period under self-limiting conditions (2 s–10 s–2 s–10 s) was obtained, as shown in Fig. 1(d). The GPC calculated from this thickness variation with ALD cycles was also similar (~0.13 nm/cycle), as observed from the self-limiting growth. The observed GPC was noticeably higher than most previously reported values for the ALD-SnS process, as shown in Table S2 [31]. In addition, the absence of any nucleation delay for SnS on the SiO_2/Si substrate indicates a fast

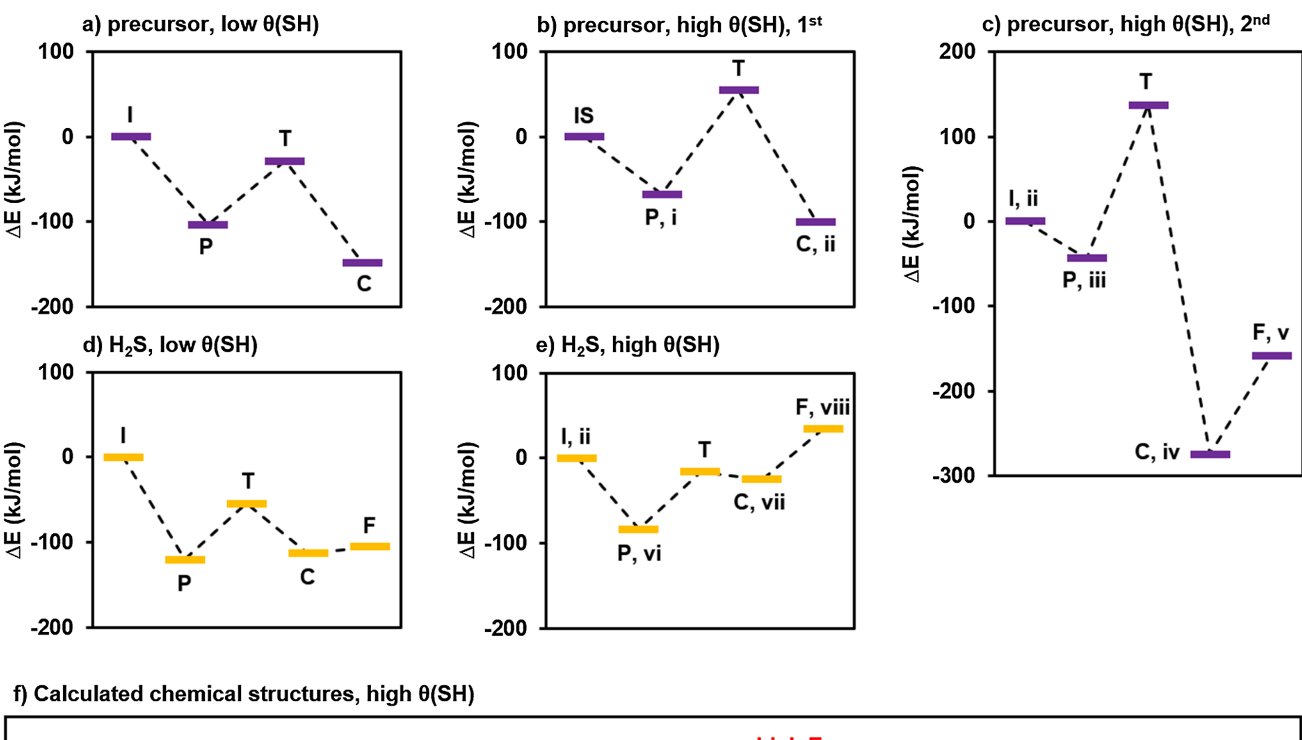

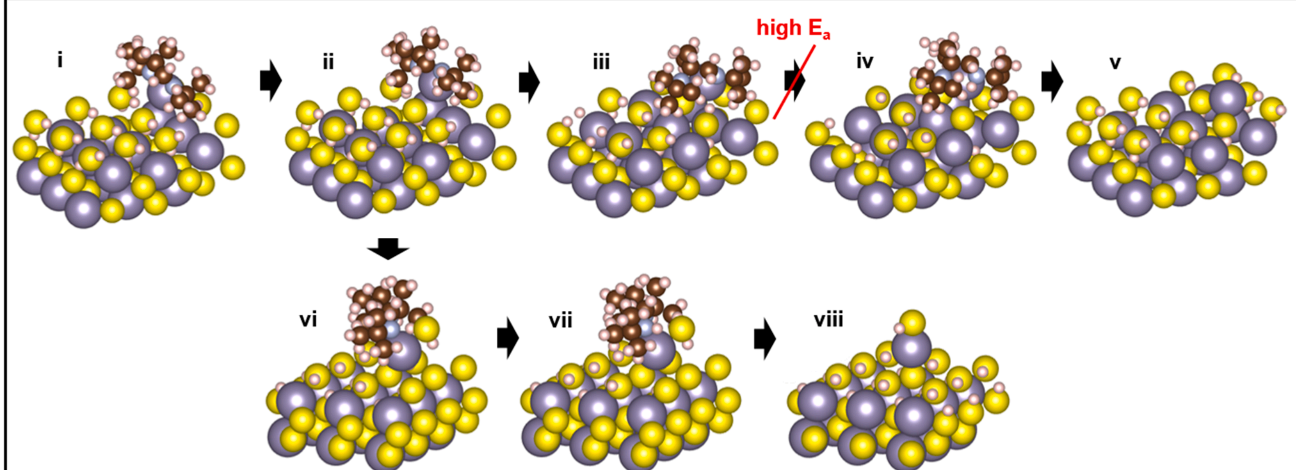

Fig. 2. Proposed reaction coordinate diagram for SnS ALD process. (a–c) Adsorption reaction of precursor, and (d, e) adsorption of H_2S; (a, d) on low thiol coverage surface, and (b, c, e) on high thiol coverage surface. (f) Calculated chemical structures of each critical points (i–viii) whose relative energy are denoted on (a–e). (I = Initial; P = Physisorption; T = Transition state, C = Chemisorption and F = Final product).

nucleation process, which would lead to produce a continuous film within a few ALD cycles for this process under consideration. Therefore, the significantly better ALD growth is attributed to the suitable properties and composition of Sn(dmpa) compared to previous precursors [41]. N,N′-di-*t*-butyl-2,3-dimethylenediamine is considered as a suitable ligand for metal organic precursors, and its bulky *tert*-butyl group on each nitrogen bounds oligomerization by steric effect [41,50,51]. When this ligand coordinates with Sn(II), it reduces the molecular weight/size of the compound (less organic ligands), resulting in a higher volatility and easier ligand removal during the reaction compared to the Sn(II) amidinate ligands. The earlier ALD-SnS process with the amidinate complex showed that two nitrogen atoms of the amidinate ligand still bonded to Sn after [Sn(amd)$_2$] reacted with the sulfhydryl moiety (-SH group) [41,44]. However, when cyclic Sn amide reacts with –SH groups on the surface, one nitrogen atom is easily released from the Sn ligand, and thus one side of the ligand moves or rotates easily [41,44]. As a result, the product of cyclic amide likely to occupy less surface space and react with a higher density of the surface sites compared to the surface reaction product of amidinate complex. Thus, by using cyclic amide-based Sn(dmpa), a better growth mechanism is expected owing to the higher vapor pressure of the liquid precursor, lower steric hindrance during the surface reaction, and ease of removal of the ligand.

DFT calculations were carried out to investigate the surface chemical reactions (low/high -SH coverage) and self-limiting nature of the Sn precursor during the SnS ALD process. Similar to the often-observed reaction mechanisms for ALD of metal sulfide materials [52], it was assumed here that a proton-transfer reaction would occur from the thiol group on the SnS substrate surface (during precursor pulse), as well as the H_2S reactant (during H_2S pulse), to the ligand of the Sn precursor. Fig. 2(a–c) show the DFT-calculated energy diagrams for the adsorption of the precursor on the substrate. It can be suggested that the surface reactions during ALD would easily occur with either low or high coverage of SH, corresponding to the relatively low process temperature experimentally observed. The initial protonation of the diamino ligand during precursor adsorption occurs with a relatively small activation energy (Ea, differences between T and P; see Fig. 2) values of 75.0 kJ/mol and 121.9 kJ/mol on the surfaces with θ(SH) = 1/9 and θ(SH) = 2, respectively [Fig. 2(a, b)]. Also, the removal of the singly protonated ligand by H_2S is suggested to be facile [Ea values of 65.8 kJ/mol and 67.5 kJ/mol on θ(SH) = 1/9 and θ(SH) = 2, respectively; Fig. 2(d, e)]. However, the diamino ligand may receive one additional proton from the remaining adjacent surface SH with high θ(SH), becoming a neutral molecule to gain a chance for desorption. However, such a reaction would be more difficult as the Ea value of 180.5 kJ/mol for such a reaction is much greater than the other possible reaction steps [Fig. 2(c)]. In other words, the diamino ligand remains on the Sn adatom originating from the Sn precursor, maintaining the self-limiting condition required for constant GPC in ALD.

3.2. Structural and compositional properties of ALD-SnS films

Several characterization tools, including XRD, RBS, XPS, and TEM, were performed to analyze the properties of the ALD-SnS films. First, grazing incidence angle X-ray diffraction (GIAXRD) with grazing angle $\omega = 2^\circ$ was performed to investigate the phase and crystallographic nature of the SnS films deposited at various temperatures, and the results are shown in Fig. 3. An optimized grazing incidence angle was first determined to observe the possible crystallinity in the films deposited at low temperature or with very low thickness (Figure S2). The obtained XRD pattern clearly shows that all the grown films were crystalline in nature. Distinctly visible and clear SnS diffraction patterns are observed for the SnS films prepared at the lowest deposition temperature of 25 °C, thus opening the possibility of using the current process toward temperature-sensitive substrates such as polymers for flexible thin film solar cell applications. The presence of both orthorhombic SnS (o-SnS) and cubic SnS (π-SnS) phases were found in the GIAXRD pattern of the SnS films, and similar observations were also found in the literature [30,37]. Furthermore, all the SnS thin films grown at different deposition temperatures showed o-SnS as the predominant phase. It can also be noticed that the SnS films grown from room temperature to 100 °C (Fig. 3a), with relatively minor peak intensities observed at 2θ values of approximately 26.5 (2 2 2) and 30.8° (4 0 0), correspond to the planes of π-SnS, which has been reported to be stable at low temperature [35,42]. Due to the complex XRD patterns or 2θ values of π-SnS and o-SnS, clear indexing is, however, not straightforward. An increase in the deposition temperature (or a thicker film) causes the cubic phase of SnS to disappear, and the major peak for the (1 1 1) plane of o-SnS becomes more dominant, which indicates the conversion of the films to a stable orthorhombic phase at higher deposition temperatures (Fig. 3b). A similar phenomenon has been observed in many previous ALD-SnS studies including solid cyclic tin precursor, where the mixed phase of π-SnS and o-SnS formed at a relatively low growth temperature favored the formation of the predominant orthorhombic phase at increased deposition temperatures [35,42]. The reason behind the transition of the crystal phase can be described by considering the surface energy alterations between several orientations of the SnS planes [36].

To study the effect of thickness on the o-SnS phase, films were prepared with different number of cycles at 125 °C, and the GIAXRD patterns of the corresponding films are shown in Figure S3. For the 100 ALD cycles (~13 nm) film, a low-intensity peak located at approximately 31.5° [corresponding to the (1 1 1) plane of o-SnS] can be clearly seen, showing the formation of only an orthorhombic phase. When the ALD reactions cycles increased to 300 (film thickness ~ 39 nm), the peak intensity of the (1 1 1) plane also increased with extra peak formation, which can be assigned to the plane of o-SnS. The intensity of the patterns further increased with increasing film thickness and became more pronounced, with other planes of o-SnS, for 1500 ALD cycles. These results suggest that the films grown at a relatively higher temperature (or

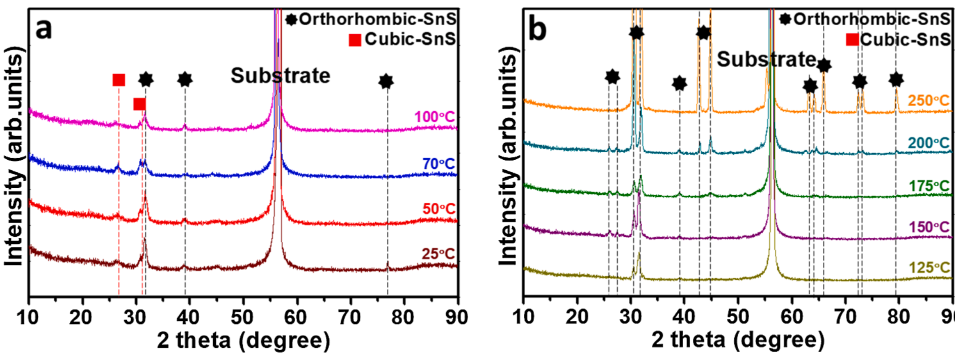

Fig. 3. GIAXRD patterns of the ALD-grown SnS films as a function of substrate temperature on Si/SiO$_2$ substrate: (a) The samples deposited from 25 to 100 °C and (b) those deposited from 125 to 250 °C.

higher thicknesses) consisted of a single o-SnS phase without change in preferential orientation. Moreover, the XRD observations clearly suggest the absence of any other possible phases of tin sulfide such as Sn_2S_3 and SnS_2, suggesting the formation of phase-pure SnS. The current ALD process, therefore, could be suitable for growing SnS-based thin film absorbers, for which any other phase except the mono-sulfide phase is considered to be an impurity phase, leading to poor solar cell performance [2,3,19].

To gain more insight into detection of the possible presence of secondary phases (SnS_2 and Sn_2S_3) in the SnS films, additional analysis through Raman spectroscopy was performed. Considering the difference in phases, we used reference values for the Raman-active frequencies in single crystals. Fig. 4 displays the Raman spectra of the samples grown at various temperatures within the frequency range of 120–350 cm^{-1}. The active modes in the Raman spectra were observed at approximately 169 (B_{2g}), 174(B_{3g}), 191(B_{2g}), 197(B_{2g}), 224 (A_g), 228 (A_g), and 294 (B_{2g}) cm^{-1}, which are related to various optical phonon modes of the o-SnS and π-SnS phases. The Raman peaks of the SnS films prepared at higher temperatures (150 °C and above) revealed peaks at approximately 169, 197, and 224 cm^{-1}, which observed from the orthorhombic phase and matched well with the reported values [34,35,42]. In the case of the films grown at low temperatures (25–100 °C), the Raman peak positions shifted considerably to higher/lower frequencies, indicating that a mixed phase of o-SnS and π-SnS formed at a comparatively low temperature. The presence of a few Raman peaks corresponding to π-SnS (191 and 202 cm^{-1}) merged with o-SnS (197 cm^{-1}) and could only be realized from the shift of the center of the peak. However, the Raman mode at 294 cm^{-1}, which is also assigned to π-SnS, clearly disappeared for the samples prepared at the higher temperature [42]. In general, the frequency of the active Raman mode in SnS obtain from the vibration of Sn against S. The frequency of these vibrational modes varies on the force constant, which in turn depends on the bonding length between the metal and chalcogen atoms. Therefore, these variations are expected in the bond lengths between tin and sulfur in the o-SnS and π-SnS phases owing to varying atomic positioning in both formations, and therefore, a slight change was observed in the Raman modes. The Raman results also suggest that the prevailing mixed phase was favored at lower temperatures, whereas only the o-SnS phase formed at a relatively higher temperatures, which is well matched with the XRD results; a similar phenomenon was observed in other studies [35,42]. The Raman spectra also show that the samples did not contain any other phase except SnS, which is usually observed at approximately 308 cm^{-1} for Sn_2S_3 and 315 cm^{-1} for SnS_2.

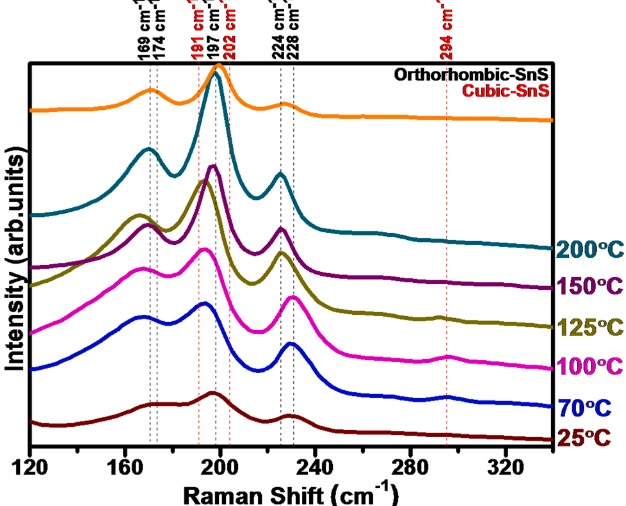

Fig. 4. Raman spectroscopy spectra of ALD-grown SnS thin films with respect to the deposition temperature on SiO_2/Si substrate.

XPS measurements were performed to further confirm the purity and valence states of the SnS films deposited at different deposition temperatures. A full spectrum survey obtained at the film surface at binding energies in the range of 0–1000 eV presented significant signs of C and O (owing to surface contamination), along with spectra conforming to various orbital electrons of tin (4d, 3d, and 3p) and S (2s, 2p). Therefore, XPS data were obtained after etching the top surface of the film for 60 s using Ar sputtering to eliminate surface contamination and to analyze the bonding status of the film more precisely. After Ar sputtering, the percentages of O and C were drastically reduced, resulting in more accurate results for Sn and S (Figure S4). The incorporation of C is occasionally noticed in films prepared from an organic ligand containing metal precursor owing to the inadequate elimination of organic ligands from the metal base at low process temperatures or to precursor decomposition at elevated deposition temperatures. Therefore, additional detailed high-resolution spectra of Sn and S were obtained after Ar sputtering. Two distinct strong peaks at 485.7 and 494.3 eV were observed in the high-resolution Sn 3d spectra [Fig. 5(a)] in the films that corresponds to Sn $3d_{5/2}$ and Sn $3d_{3/2}$, respectively. These binding energies match the divalent Sn as a result of the + 2 valence state of the Sn source used in this case [42]. There was no detection of the Sn^4 oxidation state in the spectrum, which is usually observed at a relatively higher binding energy of approximately 486.7 eV. However, the SnS film deposited at 250 °C showed one additional peak with significantly lower intensity at a lower binding energy of approximately 484.2 eV, which belonged to Sn^0. Thus, the XPS analyses indicated that the Sn–Sn metal bonding was present in the SnS film deposited at higher temperatures, probably owing to decomposition of the Sn precursor. Further, the high-resolution sulfur 2p core-level XPS spectrum at binding energies of approximately 161.3 and 162.6 eV, shown in Fig. 5(b), could be attributed to S $2p_{3/2}$ and S $2p_{1/2}$ of S^{-2} of SnS, respectively [37,42]. The presence of C and N contaminations was found to be at around ~ 2–5.2 at.% and 0.2 at.%, respectively, reflecting that there is a small amount of carbonaceous impurities in the ALD-SnS films. Additional spectra for the samples prepared at various temperatures are presented in Figure S5. Hence, assessment based on XPS analysis are also matched with conclusions made from the XRD and Raman results.

Plan-view TEM bright-field (BF) and HRTEM images and the selected area electron diffraction (SAED) pattern of the film deposited at 125 °C are shown in Fig. 6. The TEM BF image [Fig. 6(a)] shows that relatively dark-contrast grains are randomly but uniformly scattered over the surface, surrounded by bright contrast regions, suggesting that the film mostly consisted of a crystalline phase. The high-resolution TEM (HRTEM) image [Fig. 6(b)] clearly shows a well-defined crystalline nature, and clearly observed lattice spacing is observed at different positions belonging to various planes of o-SnS. The corresponding diffusion SAED ring pattern (inset) further confirms the crystalline nature of the SnS film. Additionally, cross-sectional-view TEM (XTEM) characterization was carried out to further detect the structure of the film, and the results are shown in Fig. 7. The low-magnification XTEM image reveals that the film was continuous and uniform with an elongated nanoflake-like surface. The HR-XTEM image further shows that the film was crystalline with lattice spacing in the grains.

Although the XPS analysis confirmed that the S/Sn ratio was close to 1 in the deposition temperature range of 25–200 °C [Figure S5(d)], the definite composition or stoichiometry of the ALD-SnS film (125 °C, a ALD window temperature) was measured by RBS analysis. The resultant RBS spectrum is shown in Fig. 8. Signals of backscattered ions acquired from the collision between He^{++} ions with metal Sn and sulfur components in the deposited film are evidently found at channel numbers 888 and 611, respectively. Furthermore, we can see two other backscattered signals in the spectrum of the SiO_2/Si substrate. The first one can be seen at channel number 551, originating from the collision of He++ with Si in the thermally grown SiO_2 substrate, and the second one can be seen at a lower channel number (5 2 3), which originated mainly from Si in the substrate. In addition, O was also identified in the RB spectrum at

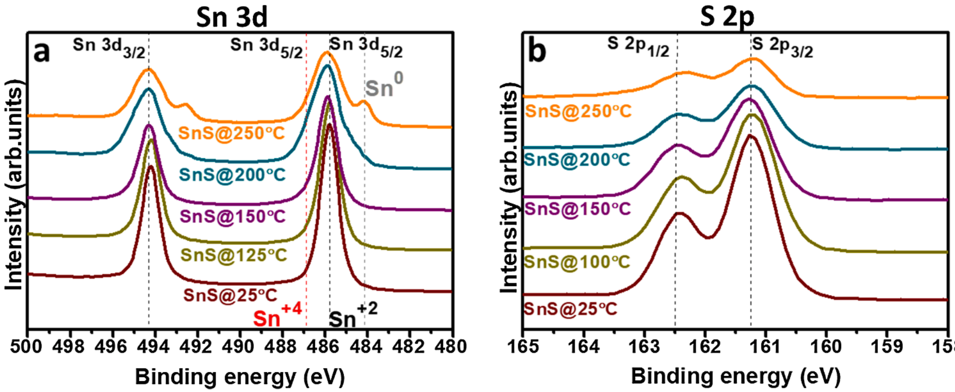

Fig. 5. High-resolution XPS spectra of (a) Sn 3d and (b) S 2p states in the ALD-grown SnS films with respect to the process temperature.

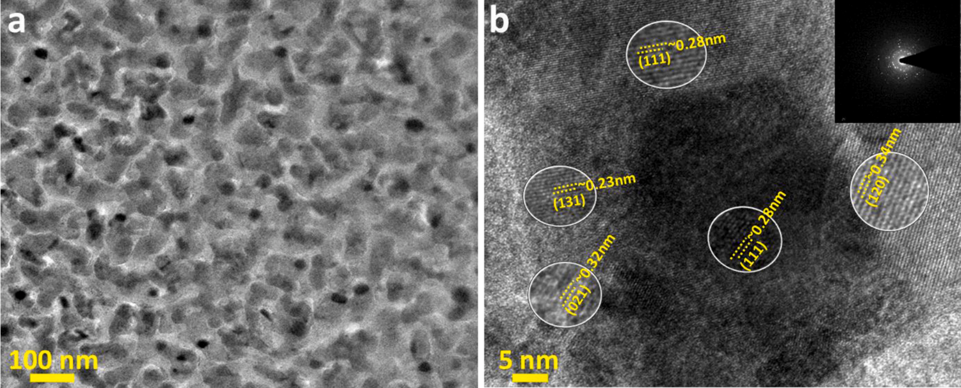

Fig. 6. (a) Plan-view TEM BF image and (b) corresponding HRTEM image of ALD-grown SnS film deposited on SiO_2/Si substrate at 125 °C. The inset is an SAED pattern representing a crystalline nature of the film.

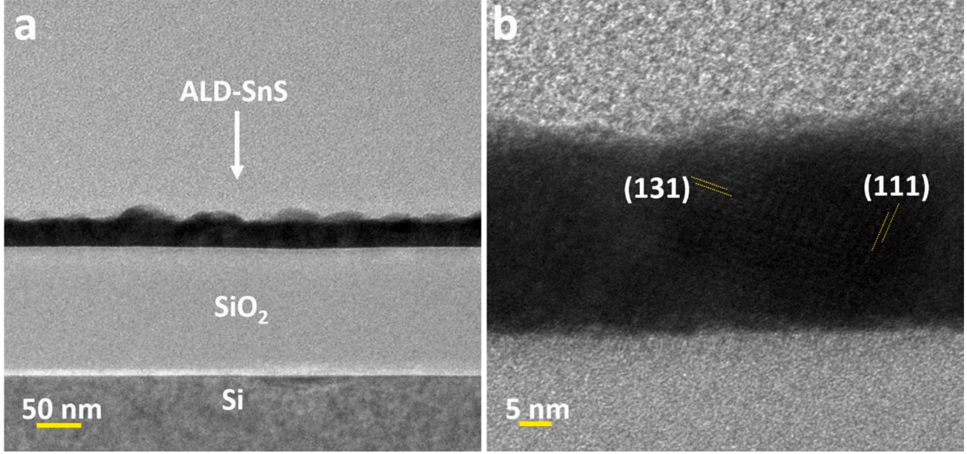

Fig. 7. Cross-sectional view (a) bright-field (BF) TEM and (b) HR-TEM image of the ALD-SnS film at 125 °C.

channel number 338, which could be attributed to the oxygen present in the SiO_2 layer. The obtained RBS spectra simulated using a RUMP model (red line) were best fitted with the experimental result (black line) when the film consisted of 50 at.% Sn and 50 at.% S. Hence, the stoichiometry of the film was determined to be exactly 1, showing the formation of tin monosulfide. Hence, the observations are in good agreement with the conclusions drawn earlier from the XRD and XPS analyses at 125 °C. The density of the SnS film grown at 125 °C was estimated by utilizing the areal density acquired from RBS analysis, the atomic mass of the constituents, and the film thickness obtained by SEM analysis. The resultant outcomes designated that the SnS film in this case had a relatively better density of 4.2 g/cm^3, which is 81% of the bulk density of SnS (5.2 g/cm^3).

The surface morphologies of the films grown at various process temperatures were studied using plan-view SEM images, which are shown in Fig. 9. Furthermore, low-magnification plane or top view SEM images (Figure S6) showed that the surfaces of the grown films up to 200 °C were continuous, uniform, and identical. Comparatively, the surface of the film grown at 250 °C appeared significantly rougher and discontinuous owing to the presence of voids on the surface. The films

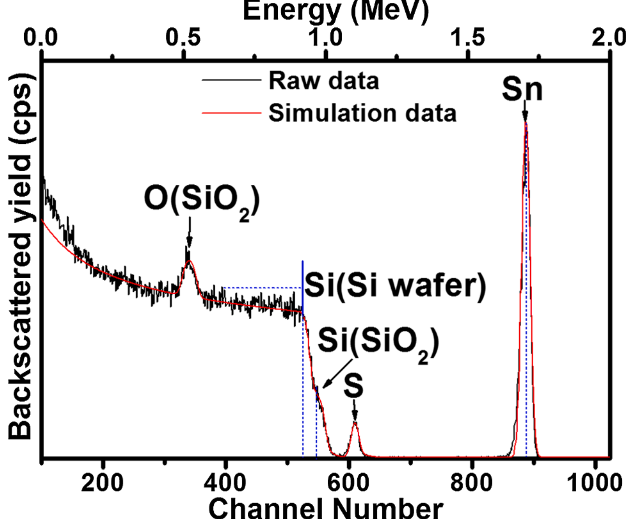

Fig. 8. RBS analysis result of the SnS film grown on the SiO_2/Si substrate using the basic pulsing condition at 125 °C.

grown at relatively low temperatures showed fairly smooth surfaces and consist with the formation of distinct flat SnS which appear as triangular or star shaped morphology without any voids [Fig. 9(a–c)]. When the substrate temperature increased, the films consisted of three types of three-dimensional (3D) growth (nanoflakes, plates, or pillar-type structures grown randomly in vertical directions) [Fig. 9(d–h)]. Such 3D growth was facilitated by increasing deposition temperature, as well as by increasing film thickness (Fig. 9 and Fig. S7). Similar switching of crystal orientation (2D to 3D growth behavior) has been observed in several earlier cases, mainly during the ALD of TMDCs [53–56] or even for metal oxides such as V_2O_5 [57]. The observed transition from two-dimensional (2D) films (in-plane orientation) to 3D islands or crystals (out-of-plane orientation) could be related to several factors such as precursor adsorption, surface energy distribution, structural distortion, stress or defect sites, *etc*. [36,53–57] For example, Sharma et *al.* have systemically discussed the switching of in-plane to out-of- plane growth mode due to the enhanced adsorption of precursor on the edge and defect sites with large number of dangling bonds during ALD growth process [53].

The same observation is also found to some extent in TMDSCs, where their dominant preferential growth in the {0 0 2} planes is followed by the presence of diverse peaks not perpendicular to the *c*-axis, which marks in the foundation of perpendicular platelets as the thickness increases [54]. In other study, the transformation of crystal orientation from parallel to perpendicular can be understood by considering the surface energies of SnS crystal planes as the {0 1 0} planes have lower surface energy than {1 0 0} and {0 0 1} planes.[36] The morphology transformation (in-plane to out-of-plane) in the present study could be a consequence of a complex interplay of various considerations as stated above, which remains to be investigated for the further study. Such growth behavior might be considered favorable in view of its application as catalysts or in energy storage devices, where a higher surface area proportionally increases the desired output of a particular application. The changes in the crystal planes, which could be determined from the appearance of a new set of XRD peaks at higher deposition temperatures or with increasing film thickness, also hints at the 3D growth of the films under certain process parameters.

Figure S8 shows SnS films with varying thicknesses or number of ALD cycles to check the grain size effect in the predominantly o-SnS layer (e.g., SnS@125 °C). The film deposited with 100 ALD cycles consists of dense and tiny grains protruding from the surface, and the size of the grains increases as the number of ALD cycles increases, which is matched with the XRD outcomes. The cross-sectional-view (Figure S7) images show that a 2D film with a relatively smooth surface was formed up to 125 °C. With increasing substrate temperature, the plan-view SEM

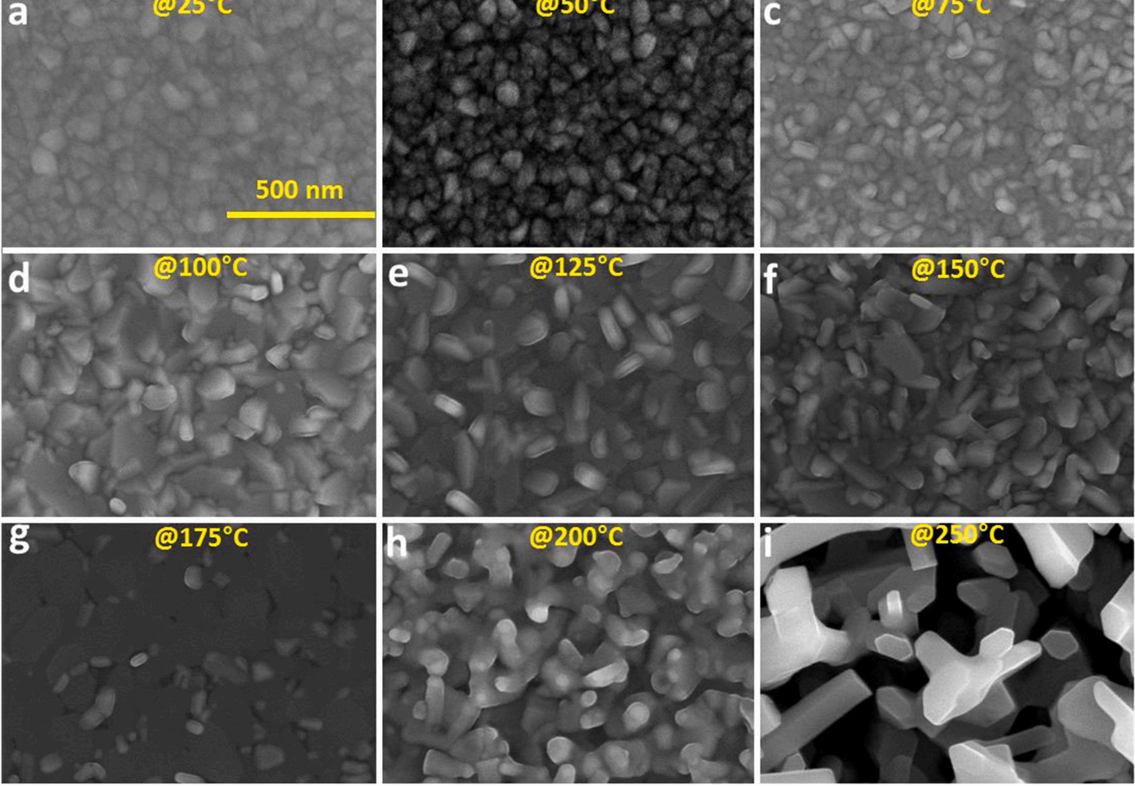

Fig. 9. Plan-view SEM images of ALD-SnS films on thermally grown SiO_2 on a Si wafer as a function of deposition temperature.

image presented in Fig. 9(i) shows elongated platelets align vertical to the substrate surface. In addition, columnar growth with long and flaky grains vertically aligned to the substrate were observed by XSEM. These elongated plate-like structures may result in high surface roughness (Figure S9). Hence, the SnS surface morphology greatly depend on the process temperature mainly due to the surface energy differences between various planes of the SnS crystal. At low growth temperature, the energetic molecules of the Sn precursor move toward the lowest surface energy position on the substrate surface and nucleate, resulting in lateral growth to the substrate to reduce the surface energy and growth along the stable (1 1 1) plane orientation. With increasing growth temperature, owing to the increased collisions among the Sn precursor molecules, the high-energy particles migrate toward multiple positions, creating stability together with the preferred (1 1 1) plane orientation. Similar results of plate- or nanoflake-like grains, which is a typical feature in the evolution of 2D materials, have also been noticed in several ALD-SnS systems from other precursors.[35,36,41,42]

3.3. Optoelectronic properties of ALD-SnS films

The above outcomes clearly demonstrate that single-phase and better-quality SnS can be successfully fabricated by the current ALD process using a novel cyclic amide Sn(II) precursor. Spectroscopic ellipsometry (SE) analysis can be used to determine the optoelectronic properties, thickness, and surface roughness of the SnS layers nondestructively without the need for contacting samples. The obtained results allow the determination of the energy band gap of the layers, as well as the specific electrical conductivity (for the conducting film), and they confirm the presence of the mixed π-SnS/o-SnS phase. These findings are important for the utilization of ALD-SnS layers in potential applications. The total thickness of the studied layer deposited using 300 ALD cycles (consisting of the thickness of the ALD-SnS layer and surface roughness) was approximately 20–35 nm for deposition temperatures up to 200 °C (see Table 2), which is consistent with the results from XRR [see Fig. 1(a)]. Considering the noticeable increase in the surface roughness for deposition temperatures higher than 200 °C as observed from SEM (Figure S7) and AFM (Figure S11), only a limited spectral range (higher wavelengths) was used for these samples, ensuring the validity of the Bruggeman effective medium approximation. The mean square error (MSE) representing the quality of the fit of the ellipsometry data, was below 5 for most of the samples. Considering the columnar-type growth, especially for the higher deposition temperatures observed from SEM for a higher number of ALD cycles (see Figure S7), the depolarization factor in the Bruggeman effective medium approximation was set close to 1 (typical for columnar growth) for samples with deposition temperatures higher than 100 °C. A Cody–Lorentz oscillator (CL) was used to describe the short-wavelength edge.[58]

$$\varepsilon_2 = \frac{E_1}{E} exp\left(\frac{E - E_g^{opt}(CL) - E_t}{E_u}\right) for 0 < E < \left(E_g^{opt}(CL) + E_t\right)$$

$$\varepsilon_2 = G(E)L(E) = \frac{\left(E - E_g^{opt}(CL)\right)^2}{\left(E - E_g^{opt}(CL)\right)^2 + E_p^2} \bullet \frac{AE_0\Gamma E}{\left[\left(E^2 - E_0^2\right)^2 + \Gamma^2 E^2\right]} for E > \left(E_g^{opt}(CL) + E_t\right)$$

$$\varepsilon_1 = E_t G(E)L(E)$$

In this model, the film is transparent below E_g^{opt} (CL) (estimation of the optical band gap). Parameters A, E_0, and Γ represent the amplitude, peak position, and broadening of the oscillator, respectively. The Cody–Lorentz model also includes an Urbach absorption term. Owing to seven free parameters, the Cody–Lorentz oscillator allows us to describe the absorption of light by different types of electron transitions between the valence and conduction bands (e.g., indirect bandgap transition and forbidden direct bandgap transition), in which the Urbach absorption term describes localized electronic states (disorder) near the valence and conduction band edges. The refractive index reported for SnS in the literature differs from that of the deposition method. Values close to 3.0 for a wavelength of 1550 nm have been reported for thermally evaporated SnS films [59,60] or the cubic (π-SnS)/orthorhombic (o-SnS) phase of SnS prepared by ALD.[35] The spectral dependence of the refractive index (left column) and extinction coefficient (right column) for ALD-SnS samples prepared at various temperatures are depicted in Fig. 10, together with the optical constants of π-SnS (simulated by three Gaussian oscillators and one polynomial spline function) and o-SnS (same functions applied for π-SnS but with different parameters) that were reported recently.[35] In particular, the absorption coefficient of o-SnS closely followed exponential Urbach-type absorption; [35] therefore, the Cody–Lorentz oscillator can be used as a model dielectric function for ALD-SnS samples. A comparison of the obtained refractive indexes and extinction coefficients of the films prepared at temperatures of 25, 50, and 70 °C with those reported for π the -SnS and o-SnS phase [35] (see first line in Fig. 10) confirmed that the studied layers contained a mix of π-SnS and o-SnS phases, in agreement with the XRD, XPS, and Raman results. For samples deposited at a temperature of 100 °C, significantly higher Urbach absorption was present. Although the refractive index was lower than expected for o-SnS, the optical constants of the samples deposited at higher temperatures were generally closer to that of o-SnS (see second line in Fig. 10), which supports the XRD, XPS, and Raman results. This allows us to conclude that the o-SnS phase was present in the studied layers deposited at higher temperatures. The values of parameter E_g^{opt} (CL), summarized in Table 2, are close to previously reported values.[2,3,5-24]

The SE results suggest that a mixture of π-SnS and o-SnS was deposited during the ALD process. To quantify the portion of each in the deposited samples, an alternative model was used for ellipsometry data evaluation in the spectral range of 300–1650 nm. The Bruggeman-type effective media approximation of π-SnS and o-SnS (optical constants of both taken from the literature [33]), together with surface roughness, were used in this model, along with a depolarization factor as one of the parameters of the fit. The results showed that the π-SnS portion decreased with increasing process temperature, and consequently, the o-SnS portion increased with increasing process temperature (see

Table 2
Layer thickness, surface roughness, total thickness, and optical bandgap E_g obtained using Cody–Lorentz oscillator, and MSE determined from UV–vis SE for SnS samples deposited by ALD for different substrate temperatures.

Deposition temperature (°C)	25	50	70	100	125	150	200	250
Thickness (nm)	25.0 ± 0.2	24.8 ± 0.2	18 ± 2	19.8 ± 0.4	14 ± 2	14 ± 1	29.5 ± 0.5	21 ± 6
Surface roughness (nm)	1.9 ± 0.2	1.5 ± 0.3	3.4 ± 0.9	6.5 ± 0.2	6 ± 2	7 ± 1	4.4 ± 0.3	57 ± 5
Total thickness (nm)	26.9 ± 0.4	26.3 ± 0.5	21 ± 3	26.3 ± 0.6	20 ± 4	21 ± 2	33.9 ± 0.8	78 ± 11
Eg (eV)	1.1 ± 0.1	1.0 ± 0.1	1.3 ± 0.1	0.8 ± 0.1	1.8 ± 0.1	1.3 ± 0.1	0.7 ± 0.1	X
MSE	3.1	2.8	3.5	5.2	11.2	11.2	4.0	3.2

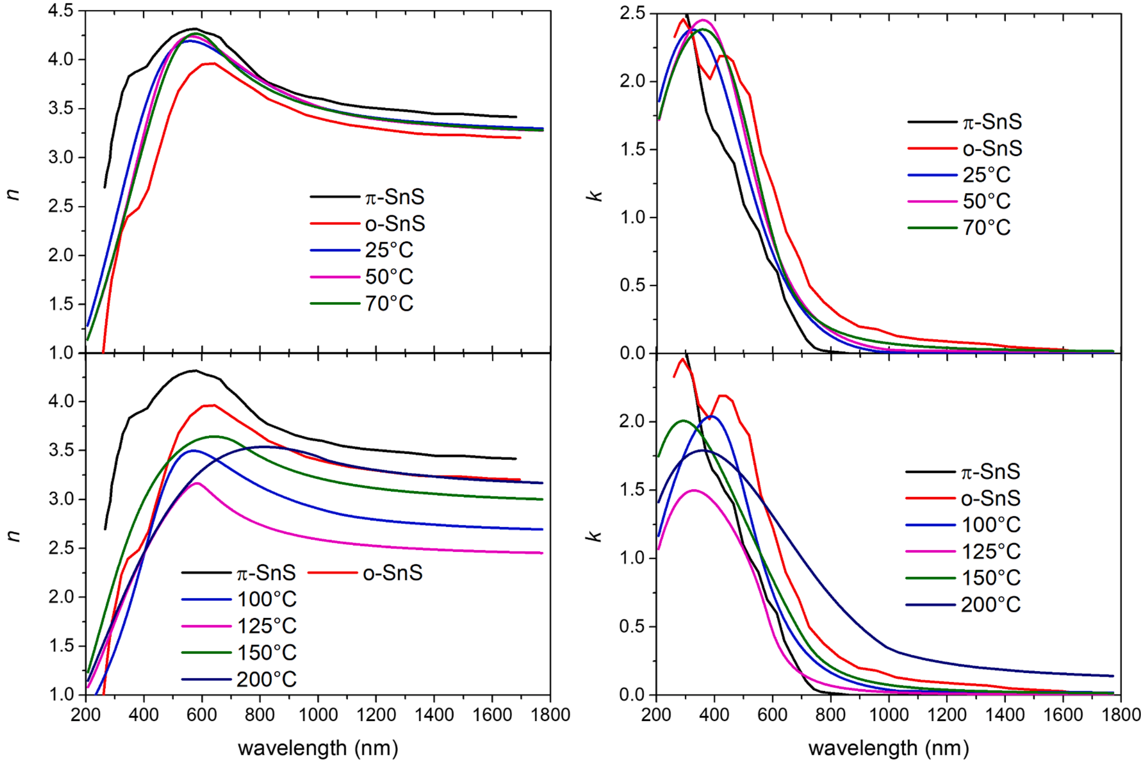

Fig. 10. Spectral dependence of refractive index *n* and extinction coefficient *k* for ALD-SnS samples deposited at different deposition temperatures in UV–vis-NIR part of spectra. Optical constants of π-SnS and o-SnS are taken from the literature.[33]

Figure S10), which is matched with the results from the XRD, XPS, and Raman analyses. It is worth mentioning that the MSE for this approach was higher (from 7.5 for ALD-SnS deposited at 25 °C to 14 for ALD-SnS deposited at 200 °C) compared with that of the model using the Cody–Lorentz oscillator. However, this approach has considerably fewer free parameters.

An increase in the extinction coefficient for higher wavelengths (λ > 3000 nm) can be alternatively modeled using a Drude oscillator or two Lorentz/Gauss oscillators (see Figure S11 as an example). To at least estimate the electrical resistivity ρ from SE data in the spectral range 1.7–7.0 µm, the Drude model describing the absorption of light on free carriers was used [61].

$$\varepsilon_{Drude} = \frac{-\hbar^2}{\varepsilon_0\rho\left(\tau E^2 + i\hbar E\right)}$$

where $\hbar$ is the Planck constant, ρ the resistivity, τ the mean scattering time, and ε_0 the permittivity of free space.

A longer wavelength allows us to determine the thickness of the samples deposited at the highest temperature (see Table 2). Electrical resistivity and mean scattering time as defined using a Drude oscillator are on the order of mΩ·cm, and femtoseconds (fs), respectively, and the values do not significantly change, even at higher deposition temperatures (MSE ≈ 5).

It is worth mentioning that the determined specific electrical resistivity ρ and mean scattering time τ depend on the spectral range used for the evaluation of ellipsometry data [ρ decreases by approximately half (e.g., from 11 to 5 mΩ·cm) and τ increases approximately two time (e.g., 2.5 instead of 1.1 fs) when a spectral range of up to 10 µm is used] and gives only order estimation.

It is known that the SE is sensitive to some materials properties including layer thickness, surface roughness, optical anisotropy. However, the interpretation of data acquired by ellipsometry (ellipsometric angles Ψ and Δ) is quite complicated and needs a construction of an applicable model. Four-point probe was also used for measuring the resistivity of the SnS films as a function of deposition temperature. Significant difference (by several orders) between the electrical resistivities obtained from ellipsometry and four-point probe can be noticed. Using four-point measurement the highest electrical resistivity of about ~ 648 Ω·cm was obtained for the film grown at room temperature (25 °C), and the resistivity significantly decreased to 351–137 Ω·cm with increasing deposition temperature from 100 to200 °C. The values of resistivity obtained from four-point method agree with those reported in the literature [36,37,62,63]. In general, the variation in the resistivity depends on the crystal structure, grain size, intrinsic stress and lattice defects interstitials and presence of binary phases of the films. In this study, the variations in resistivity of the films correlate mainly with the crystal structure, crystallinity, and morphology (in-plane to out-of-plane). The film deposited at 25 °C or thinner films (please see the Fig. 1(a)) demonstrates high resistivity might be due to the existence of higher number of lattice defects, poor crystallinity, and existence of several inter-crystalline regions, which influence the evolution of grains to a big size. On the other hand, at higher deposition temperature (or thicker films), the crystallinity is increased, and the grains are comparatively increased that permit the less carriers scattering and carriers move easily in the lattice leading a decline in resistivity. The reduction in the resistivity values with increase of deposition temperature (or film thickness) have been stated in several reports [18,36,37,60,61].

Taking both described disagreements into account using the simple Drude model is probably inappropriate in our case. Therefore, two Gaussian oscillators describing the absorption of light by lattice phonons with amplitude *A*, position *E*, and broadening B_r as free parameters of each were used for the estimation of ellipsometry data in the infrared region of the spectra. The change in the π-SnS/o-SnS ratio with deposition temperature observed from the UV–vis-NIR part of the spectra did not significantly change the position of the lattice phonon absorption or the long-wavelength absorption edge, which are dependent on the first approximation of the mass and bond strength between atoms. There was

a noticeable increase in the amplitude of both oscillators with increasing temperature (from 25 to 125 °C), followed by a decrease in the amplitude of both oscillators at higher deposition temperatures, suggesting that the strongest absorption of light by lattice phonons occurred when the π-SnS/o-SnS ratio was approximately 1. When the π-SnS or o-SnS phase prevailed in the sample, the phonon spectrum of the lattice was poorer, leading to lower light absorption. The absorption peak at ≈1600–1800 cm^{-1}/1200 cm^{-1} (8300 nm) can be alternatively assigned to C═O stretching, S═O stretching, or C—O stretching. The presence of these bonds could be caused by the physisorbed and chemisorbed water reported in the literature for SnS films prepared by the SILAR method [64]. However, a monotonic dependence on the deposition temperature is expected in the case of absorption of light by physisorbed and chemisorbed water [64]. The thicknesses of the samples deposited at the highest deposition temperature obtained using two Gaussian oscillators as the model dielectric function is summarized in Table 2. A comparison of the refractive index n and extinction coefficient k obtained using the Drude oscillator, the Gaussian oscillator, and point-by-point fit in the infrared region of the spectra is depicted in Figure S11 for the samples deposited at 50 °C. The results appear almost identical for the other deposition temperatures. Based on the previous discussion, the combination of a Cody–Lorentz oscillator describing the short-wavelength absorption edge and two Gaussian oscillators describing the absorption of light on lattice phonons/chemical bonds was used as the model dielectric function in a broad spectral range (from 200 nm to 10,000 nm). The resultant optical constants of ALD-SnS are summarized in Fig. 11 (MSE ≈ 5). Notice the semi-transparent region ($k > 0$) from ≈ 900 nm to 3500 nm. The semiconducting properties of ALD-SnS, associated with the above-cited SnS properties, make solar cell applications of this material possible. We will carry out future work based on the present results.

4. Summary and conclusions

A thermal ALD process for phase-pure and crystalline SnS thin films at low temperatures (25–250 °C) was established using a novel cyclic amide precursor, N,N′-di (t-butyl)-2-methyl-1,2-propanediamino tin(II) [Sn(dmpa)] and H_2S as a reactant. Although the crystalline SnS films could be grown at room temperature, the use of a divalent precursor also permitted the formation of SnS (Sn^{2+}) within a wide range of temperatures. The self-limiting ALD growth regime was confirmed with both the precursor and reactant dosing condition during the process, showing a significantly high GPC of 0.13 nm. DFT calculations predicted the surface reaction mechanism of the precursor and H_2S, as well as possible self-limiting growth behavior. The SnS film deposited at low temperature (25–100 °C) contained a mixed phase of cubic and orthorhombic SnS, whereas phase-pure orthorhombic SnS was dominant at increased growth temperatures (125–250 °C). Amorphous and secondary phases were not detected by Raman spectroscopy or XRD, which was further supported by TEM analysis. RBS and XPS results confirmed the formation of well stoichiometric of tin monosulfide (S/Sn = 1) phase with a small amount of carbon impurity (~2 at. %). The SEM analysis revealed that 3D nanoflakes/pillars grew with increasing deposition temperature and increasing film thickness, resulting in a very rough film surface. A relatively broad semi-transparent window (from ≈ 900 nm to 3500 nm), no significant light absorption on free carriers, an energy bandgap of approximately 1.1 eV were observed using SE analysis. In short, the current study offers a single-phase, high-quality ALD-SnS process at a relatively low deposition temperature and in-depth analysis of the deposited films opens the possibility of using them in various applications, especially as an absorber material in thin film solar cell.

CRediT authorship contribution statement

Mohd Zahid Ansari: Methodology, Investigation, Data curation, Writing – original draft, Visualization. **Petr Janicek:** Formal analysis, Data curation, Writing – review & editing. **Dip K. Nandi:** Writing – review & editing. **Stanislav Slang:** Investigation. **Marek Bouska:** Investigation. **Hongjun Oh:** Software, Writing – review & editing. **Bonggeun Shong:** Software, Writing – review & editing. **Soo-Hyun Kim:** Methodology, Investigation, Data curation, Writing – original draft, Visualization, Resources, Conceptualization, Supervision, Funding

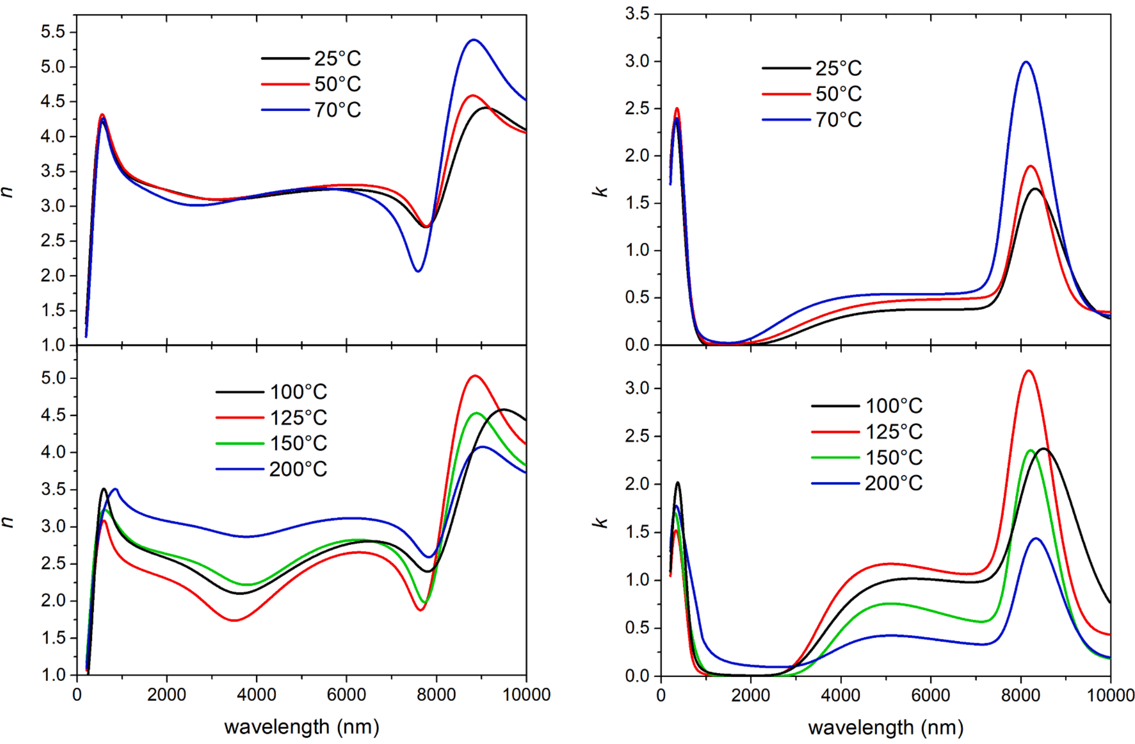

Fig. 11. Spectral dependence of refractive index n and extinction coefficient k for ALD-SnS samples deposited at different temperatures across a broad spectral range.

acquisition, Writing – review & editing.

Declaration of Competing Interest

The authors declare that they have no known competing financial interests or personal relationships that could have appeared to influence the work reported in this paper.

Acknowledgments

This work was supported by the National Research Foundation of Korea (NRF) grant funded by the Korea government (MSIT) (2021R1A2C1007601). The authors appreciated the financial support from grant LM2018103 by the Ministry of Education, Youth, and Sports of the Czech Republic. The precursor used in this study was provided by Hansol Chemical Co. Ltd., Korea.

Appendix A. Supplementary material

Supplementary information accompanies this paper at https://www.sciencedirect.com/journal/applied-surface-science. This content provides additional details about: Chemical structure of the precursor, DFT-calculated geometries, XRD analysis at various incident angles, XRD results as a function of ALD cycles, Wide-scan XPS spectra, High-resolution XPS spectra, Low magnification plan-view SEM images, Cross-sectional view SEM images, Plan-view SEM images as a function of ALD cycles, 2D AFM images, π-SnS and o-SnS calculated by spectroscopic ellipsometry, and Comparison of optical constants in IR part.

Supplementary data to this article can be found online at https://doi.org/10.1016/j.apsusc.2021.150152.

References

[1] M.R. Gao, Y.F. Xu, J. Jiang, S.H. Yu, Nanostructured metal chalcogenides: synthesis, modification, and applications in energy conversion and storage devices, Chem. Soc. Rev. 42 (2013) 2986–3017, https://doi.org/10.1039/C2CS35310E.
[2] P. Shinde, S.C. Rout, Advances in synthesis, properties and emerging applications of tin sulfides and its heterostructures, Mater. Chem. Front. 5 (2021) 516–556, https://doi.org/10.1039/d0qm00470g.
[3] R.E. Banai, M.W. Horn, J.R.S. Brownson, A review of tin (II) monosulfide and its potential as a photovoltaic absorber, Sol. Energy Mater Sol. Cells 150 (2016) 112–129, https://doi.org/10.1016/j.solmat.2015.12.001.
[4] J.H. Han, Y.J. Chung, B.K. Park, S.K. Kim, H.-S. Kim, C.G. Kim, T.-M. Chung, Growth of p-type tin (II) monoxide thin films by atomic layer deposition from bis (1-dimethylamino-2-methyl- 2propoxy)tin and H_2O, Chem. Mater. 26 (2014) 6088–6091, https://doi.org/10.1021/cm503112v.
[5] W. Albers, C. Haas, H.J. Vink, J.D. Wasscher, Investigations on SnS, J. Appl. Phys. 32 (1961) 2220–2225, https://doi.org/10.1063/1.1777047.
[6] N. Revathi, S. Bereznev, M. Loorits, J. Raudoja, J. Lehner, J. Gurevits, R. Traksmaa, V. Mikli, E. Mellikov, O. Volobujeva, Annealing effect for SnS thin films prepared by high-vacuum evaporation, J. Vac. Sci. Technol. A 32 (2014), 061506, https://doi.org/10.1116/1.4896334.
[7] S.D. Mare, M. Menossi, A. Salavei, E. Artegiani, F. Piccinelli, A. Kumar, G. Mariotto, A. Romeo, SnS thin film solar cells: perspectives and limitations, Coatings 7 (2017) 34, https://doi.org/10.3390/coatings7020034.
[8] D. Sharma, N. Kamboj, K. Agarwal, B.R. Mehta, Structural, optical and photoelectrochemical properties of phase pure Sn_S and SnS_2 thin films prepared by vacuum evaporation method, J. Alloy Compd. 822 (2020), 153653, https://doi.org/10.1016/j.jallcom.2020.153653.
[9] S.S. Hegde, A.G. Kunjomana, K.A. Chandrasekharan, K. Ramesh, M. Prashantha, Optical and electrical properties of SnS semiconductor crystals grown by physical vapor deposition technique, Physica B 406 (2011) 1143–1148, https://doi.org/10.1016/j.physb.2010.12.068.
[10] S. Cheng, G. Conibeer, Physical properties of very thin SnS films deposited by thermal evaporation, Thin Solid Films 520 (2011) 837–841, https://doi.org/10.1016/j.tsf.2011.01.355.
[11] M. Devika, N. Koteeswara Reddy, M. Prashantha, K. Ramesh, S. Venkatramana Reddy, Y.B. Hahn, K.R. Gunasekhar, The physical properties of SnS films grown on lattice-matched and amorphous substrates, Phys. Status Solidi A 207 (2010) 1864–1869, https://doi.org/10.1002/pssa.200925379.
[12] M. Devika, N. Koteeswara Reddy, K. Ramesh, V. Ganesan, E.S.R. Gopal, K. T. Ramakrishna Reddy, Influence of substrate temperature on surface structure and electrical resistivity of the evaporated tin sulphide films, Appl. Surf. Sci. 253 (2006) 1673–1676, https://doi.org/10.1016/j.apsusc.2006.03.005.
[13] K. Hartman, J.L. Johnson, M.I. Bertoni, D. Recht, M.J. Aziz, M.A. Scarpulla, T. Buonassisi, SnS thin-films by RF sputtering at room temperature, Thin Solid Films 519 (2011) 7421–7424, https://doi.org/10.1016/j.tsf.2010.12.186.
[14] J. Malaquias, P.A. Fernandes, P.M.P. Salomé, A.F. da Cunha, Assessment of the potential of tin sulphide thin films prepared by sulphurization of metallic precursors as cell absorbers, Thin Solid Films 519 (2011) 7416–7420, https://doi.org/10.1016/j.tsf.2011.01.393.
[15] L. Zhao, Y. Di, C. Yan, F. Liu, Z. Cheng, L. Jiang, X. Hao, Y. Lai, J. Li, In situ growth of SnS absorbing layer by reactive sputtering for thin film solar cells, RSC Adv. 6 (2016) 4108, https://doi.org/10.1039/c5ra24144h.
[16] V.K. Arepalli, J. Kim, Effect of substrate temperature on the structural and optical properties of radio frequency sputtered tin sulfide thin films for solar cell application, Thin Solid Films 666 (2018) 34–39, https://doi.org/10.1016/j.tsf.2018.09.009.
[17] V.K. Arepalli, Y. Shin, J. Kim, Photovoltaic behavior of the room temperature grown RF-Sputtered SnS thin films, Opt. Mater. 88 (2019) 594–600, https://doi.org/10.1016/j.optmat.2018.12.016.
[18] S.-I. Son, D. Shin, Y.G. Son, C.S. Son, D.R. Kim, J.H. Park, S. Kim, D. Hwang, P. Song, Effect of working pressure on the properties of RF sputtered SnS thin films and photovoltaic performance of SnS-based solar cells, J. Alloy Compd. 831 (2020), 154626, https://doi.org/10.1016/j.jallcom.2020.154626.
[19] P. Sinsermsuksakul, L. Sun, S.W. Lee, H.H. Park, S.B. Kim, C. Yang, R.G. Gordon, Overcoming efficiency limitations of SnS-based solar cells, Adv. Energy Mater. 4 (2014) 1400496, https://doi.org/10.1002/aenm.201400496.
[20] W. Sun, X. Rui, D. Yang, Z. Sun, B. Li, W. Zhang, Y. Zong, S. Madhavi, S. Dou, Q. Yan, Two-dimensional tin disulfide nanosheets for enhanced sodium storage, ACS Nano 9 (2015) 11371–11381, https://doi.org/10.1021/acsnano.5b05229.
[21] L. Zhang, Y. Huang, Y. Zhang, W. Fan, T. Liu, Three dimensional nanoporous graphene-carbon nanotube hybrid frameworks for confinement of SnS_2 nanosheets: flexible and binder-free papers with highly reversible lithium storage, ACS Appl. Mater. Interfaces 7 (2015) 27823–27830, https://doi.org/10.1021/acsami.5b09115.
[22] See supplementary information for Table S1 & S2.
[23] T.G. Hibbert, M.F. Mahon, K.C. Molloy, L.S. Price, I.P. Parkin, Deposition of tin sulfide thin films from novel, volatile (fluoroalkythiolato) tin(IV) precursors, J. Mater. Chem. 11 (2001) 469, https://doi.org/10.1039/B005863G.
[24] I.P. Parkin, L.S. Price, a T.G. Hibbertb, K.C. Molloy, The first single source deposition of tin sulfide coatings on glass: aerosol-assisted chemical vapour deposition using $[Sn(SCH_2CH_2S)_2]$, J. Mater. Chem. 11 (2001) 1486–1490, https://doi.org/10.1039/b009923f.
[25] L.C. Price, I.P. Parkin, A.M.E. Hardy, R.J.H. Clark, Atmospheric pressure chemical vapor deposition of tin sulfides (SnS, Sn_2S_3, and SnS_2) on glass, Chem. Mater. 11 (1999) 1792–1799, https://doi.org/10.1021/cm990005z.
[26] B.P. Bade, S.S. Garje, Y.S. Niwate, M. Afzaal, P. O'Brien, Tribenzyltin(IV)chloride thiosemicarbazones: novel single source precursors for growth of SnS thin films, Chem. Vap. Deposition 14 (2008) 292–295, https://doi.org/10.1002/cvde.200806687.
[27] J. Park, M. Song, W.M. Jung, W.Y. Lee, J. Lee, H. Kim, I.-W. Shim, Preparation of SnS thin films by MOCVD method using single source precursor, Bis(3-mercapto-1-propanethiolato) Sn(II), Bull. Korean Chem. Soc. 33 (2012) 3383, https://doi.org/10.5012/bkcs.2012.33.10.3383.
[28] I.Y. Ahmet, M.S. Hill, A.L. Johnson, L.M. Peter, Polymorph-selective deposition of high purity SnS thin films from a single source precursor, Chem. Mater. 27 (2015) 7680–7688, https://doi.org/10.1021/acs.chemmater.5b03220.
[29] A.L. Catherall, S. Harris, M.S. Hill, A.L. Johnson, A.F. Mahon, Deposition of SnS thin films from Sn(II) thioamidate precursors, Cryst. Growth Des. 17 (2017) 5544–5551, https://doi.org/10.1021/acs.cgd.7b01100.
[30] H. Zhang, Y. Balaji, A.N. Mehta, M. Heyns, M. Caymax, I. Radu, W. Vandervorstbd, A. Delabie, Formation mechanism of 2D SnS_2 and SnS by chemical vapor deposition using $SnCl_4$ and H_2S, J. Mater. Chem. C 6 (2018) 6172, https://doi.org/10.1039/c8tc01821a.
[31] M. Al-Shakban, P.D. Matthews, E.A. Lewis, J. Raftery, I. Vitorica-Yrezabal, S. J. Haigh, D.J. Lewis, P. O'Brien, Chemical vapor deposition of tin sulfide from diorganotin(IV) dixanthates, J. Mater. Sci. 54 (2019) 2315–2323, https://doi.org/10.1007/s10853-018-2968-y.
[32] M.Z. Ansari, D.K. Nandi, R. Janicek, S.A. Ansari, R. Ramesh, R.T. Cheon, B. Shong, S.-H. Kim, Low-temperature atomic layer deposition of highly conformal tin nitride thin flms for energy storage devices, ACS Appl. Mater. Interfaces 11 (2019) 43608–43621, https://doi.org/10.1021/acsami.9b15790.
[33] M.Z. Ansari, N. Parveen, D.K. Nandi, R. Ramesh, S.A. Ansari, T. Cheon, S.-H. Kim, Enhanced activity of highly conformal and layered tin sulfide (SnS_x) prepared by atomic layer deposition (ALD) on 3D metal scaffold towards high performance supercapacitor electrode, Sci. Rep. 9 (2019) 10225, https://doi.org/10.1038/s41598- 019-46679-7.
[34] J.Y. Kim, S.M. George, Tin monosulfide thin films grown by atomic layer deposition using tin 2,4-pentanedionate and hydrogen sulfide, J. Phys. Chem. C 114 (2010) 17597–17603, https://doi.org/10.1021/jp9120244.
[35] O.V. Bilousov, Y. Ren, T. Törndahl, O. Donzel-Gargand, T. Ericson, C. Platzer-Björkman, M. Edoff, C. Hagglund, Atomic layer deposition of cubic and orthorhombic phase tin monosulfide, Chem. Mater. 29 (2017) 2969–2978, https://doi.org/10.1021/acs.chemmater.6b05323.
[36] P. Sinsermsuksakul, J. Heo, W. Noh, A.S. Hock, R.G. Gordon, Atomic layer deposition of tin monosulfide thin films, Adv. Energy Mater. 1 (2011) 1116–1125, https://doi.org/10.1002/aenm.201100330.

[37] G. Ham, S. Shin, J. Park, H. Choi, J. Kim, Y.-A. Lee, H. Seo, H. Jeon, Tuning the electronic structure of tin sulfides grown by atomic layer deposition, ACS Appl. Mater. Interfaces 5 (2013) 8889–8896, https://doi.org/10.1021/am401127s.

[38] H.H. Park, R. Heasley, S.L. Steinmann, R.V. Jaramillo, K. Hartman, R. Chakraborty, P. Sinsermsuksakul, D. Chua, T. Buonassisi, R.G. Gordon, Co-optimization of SnS absorber and Zn(O, S) buffer materials for improved solar cells, Prog. Photovolt: Res. Appl. 23 (2015) 901–908, https://doi.org/10.1002/pip.2504.

[39] B. Jang, S. Yeo, H. Kim, B. Shin, S.-H. Kim, Fabrication of single-phase SnS film by H_2 annealing of amorphous SnS_x prepared by atomic layer deposition, J. Vac. Sci. Technol. A 35 (2017), 031506, https://doi.org/10.1116/1.4978892.

[40] H. Choi, J. Lee, S. Shin, J. Lee, S. Lee, H. Park, S. Kwon, N. Lee, M. Bang, S.-B. Lee, H. Jeon, Fabrication of high crystalline SnS and SnS_2 thin films, and their switching device characteristics, Nanotechnology 29 (2018), 215201, https://doi.org/10.1088/1361-6528/aab3c1.

[41] S.B. Kim, P. Sinsermsuksakul, A.S. Hock, R.D. Pike, R.G. Gordon, Synthesis of N-heterocyclic stannylene (Sn(II)) and germylene (Ge(II)) and a Sn(II) amidinate and their application as precursors for atomic layer deposition, Chem. Mater. 26 (2014) 3065–3073, https://doi.org/10.1021/cm403901y.

[42] I.-H. Baek, J.J. Pyeon, Y.G. Song, T.-M. Chung, H.-R. Kim, S.-H. Baek, J.-S. Kim, C.-Y. Kang, J.-W. Choi, C.S. Hwang, J.H. Han, S.K. Kim, Synthesis of SnS thin films by atomic layer deposition at low temperatures, Chem. Mater. 29 (2017) 8100–8110, https://doi.org/10.1021/acs.chemmater.7b01856.

[43] Organometallic precursor composition for atomic layer deposition (ald), and ald deposition method using same. https://patents.google.com/patent/WO2017090854A1.

[44] S.B. Kim, X. Zhao, L.M. Davis, A. Jayaraman, C. Yang, R.G. Gordon, Atomic layer deposition of tin monosulfide using vapor from liquid bis(N, N′ diisopropylformamidinato)tin(II) and $_H$2S, ACS Appl. Mater. Interfaces 11 (2019) 45892–45902, https://doi.org/10.1021/acsami.9b16933.

[45] J.-W. Choi, J. Oh, T.T. Ngoc Van, J. Kim, H. Hwang, C.G. Kim, T.-M. An, K.-S. Chung, B. Shong, J.-H. Hwang, Tin oxysulfide composite thin films based on atomic layer deposition of tin sulfide and tin oxide using $Sn(Dmamp)_2$ as Sn Precursor, Ceram. Int. 46 (2020) 5109–5118, https://doi.org/10.1016/j.ceramint.2019.10.254.

[46] G. Kresse, J. Furthmüller, Efficient iterative schemes for ab initio total-energy calculations using a plane-wave basis set, Phys. Rev. B 54 (1996) 11169, https://doi.org/10.1103/PhysRevB.54.11169.

[47] G. Henkelman, H. Jónsson, A climbing image nudged elastic band method for finding saddle points and minimum energy paths, J. Chem. Phys. 113 (2000) 9901–9904, https://doi.org/10.1063/1.1329672.

[48] C.M. Herzinger, B. Johs, W.A. McGahan, J.A. Woollam, W. Paulson, Ellipsometric determination of optical constants for silicon and thermally grown silicon dioxide via a multi-sample, multi-wavelength, multi-angle investigation, J. Appl. Phys. 83 (1998) 3323–3336, https://doi.org/10.1063/1.367101.

[49] D.A.G. Bruggeman, Berechnung verschiedener physikalischer Konstanten von heterogenen substanzen, Ann. Phys. (Leipzig) 24 (1935) 636–679, https://doi.org/10.1002/andp.19354160705.

[50] W. Li, N.J. Hill, A.C. Tomasik, G. Bikzhanova, R. West, A new monomerics N-heterocyclic silylene as a racemic mixture, Organometallics 25 (2006) 3802, https://doi.org/10.1021/om060544v.

[51] S.M. Mansell, R.H. Herber, I. Nowik, D.H. Ross, C.A. Russell, D.F. Wass, Coordination chemistry of N-heterocyclic stannylenes: A combined synthetic and mössbauer spectroscopy study, Inorg. Chem. 50 (2011) 2252, https://doi.org/10.1021/ic101920x.

[52] N.P. Dasgupta, X. Meng, J.W. Elam, A.B.F. Martinson, Atomic layer deposition of metal sulfide materials, Acc. Chem. Res. 48 (2015) 341–348, https://doi.org/10.1021/ar500360.

[53] A. Sharma, M.A. Verheijen, L. Wu, S. Karwal, V. Vandalon, H.C.M. Knoops, R. S. Sundaram, J.P. Hofmann, W.M.M. (Erwin) Kessels, A.A. Bol, Low-temperature plasma-enhanced atomic layer deposition of 2-D MoS_2: large area, thickness control and tuneable morphology, Nanoscale 10 (2018) 8615–8627, https://doi.org/10.1039/c8nr02339e.

[54] D.K. Nandi, S. Yeo, M.Z. Ansari, S. Sinha, T. Cheon, J. Kwon, H. Kim, J. Heo, T. Song, S.-H. Kim, Thickness-dependent electrochemical response of plasma enhanced atomic layer deposited WS_2 anodes in Na-ion battery, Electrochim. Acta 322 (2019) 1347662, https://doi.org/10.1016/j.electacta.2019.134766.

[55] M.B. Sreedhara, S. Gope, B. Vishal, R. Datta, A.J. Bhattacharyya, C.N.R. Rao, Atomic layer deposition of crystalline epitaxial MoS_2 nanowall networks exhibiting superior performance in thin-film rechargeable Na-ion batteries, J. Mater. Chem. A 6 (2018) 2302–2310, https://doi.org/10.1039/C7TA09399C.

[56] H. Zhang, T. van Pelt, A.N. Mehta, H. Bender, I. Radu, M. Caymax, W. Vandervorst, A. Delabie, Nucleation and growth mechanism of 2D SnS_2 by chemical vapor deposition: initial 3D growth followed by 2D lateral growth, 2D Mater. 5 (2018), 035006, https://doi.org/10.1088/2053-1583/aab853.

[57] E. Østreng, K.B. Gandrud, Y. Hu, O. Nilsen, H. Fjellvåg, High power nano-structured V2O5 thin film cathodes by atomic layer deposition, J. Mater. Chem. A 2 (2014) 15044–15051, https://doi.org/10.1039/C4TA00694A.

[58] A.S. Ferlauto, G.M. Ferreira, J.M. Pearce, C.R. Wronski, R.W. Wronski, X. Deng, G. Ganguly, Analytical model for the optical functions of amorphous semiconductors from the near-infrared to ultraviolet: Applications in thin film photovoltaics, J. Appl. Phys. 92 (2002) 2424, https://doi.org/10.1063/1.1497462.

[59] M.M. El-Nahass, H.M. Zeyada, M. SAziz, N.A El-Ghamaz, Optical properties of thermally evaporated SnS thin films, Optical properties of thermally evaporated SnS thin films, Opt. Mater. 20 (2002) 159–170, https://doi.org/10.1016/S0925-3467(02)00030-7.

[60] M. Devika, N. Koteeswara Reddy, K. Ramesh, R. Ganesan, K.R. Gunasekhar, E.S. R. Gopal, K.T. Ramakrishna Reddy, Thickness effect on the physical properties of evaporated SnS films, J. Electrochem. Soc. 154 (2007) H67, https://doi.org/10.1149/1.2398816.

[61] T.E. Tiwald, D.W. Thompson, J.A. Woollam, W. Paulson, R. Hance, Application of IR Variable Angle Spectroscopic Ellipsometry to the Determination of Free Carrier Concentration Depth Profiles, Thin Solid Films 313–314 (1998) 661–666.

[62] N.K. Reddy, K.T.R. Reddy, Preparation and characterisation of sprayed tin sulphide films grown at different precursor concentrations, Mater. Chem. Phys. 102 (2007) 13–18, https://doi.org/10.1016/j.matchemphys.2006.10.009.

[63] E. Guneri, C. Ulutas, F. Kirmizigul, G. Altindemir, F. Gode, C. Gumus, Effect of deposition time on structural, electrical, and optical properties of SnS thin films deposited by chemical bath deposition, Appl. Surf. Sci. 257 (2010) 1189–1195, https://doi.org/10.1016/j.apsusc.2010.07.104.

[64] G.H. Chao, T. Shen, L. Wu, L. Zhang, F. Jiang, Preparation and the growth mechanism of zinc blende structure tin sulfide films by successive ionic layer adsorption and reaction, J. Cryst. Growth 312 (2010) 3009–3013, https://doi.org/10.1016/j.jcrysgro.2010.07.001.